Range and resolution analysis of wide-azimuth angle decomposition

Gabriela Melo and Paul Sava
Center for Wave Phenomena, Colorado School of Mines, Golden, CO 80401

ABSTRACT

Imaging in complex media benefits from uniform illumination of the target from all possible directions. Moreover, it is desirable to recover reflectivity from seismic data as a function of incidence and azimuthal angles at every location over the reflector. Applications of angle-dependent reflectivity include velocity and anisotropy estimation and amplitude versus angle (AVA) analysis. One way of constructing angle-dependent reflectivity is to apply an extended imaging condition to the extrapolated source and receiver wavefields. This imaging condition allows one to construct images as a function not only of three-dimensional position but also space-lags of the source/receiver wavefield cross-correlation. The information in the space-lag domain can be mapped into the angle-domain, defined by the reflection and azimuthal angles, at every image point. The relationship between sampling parameters in the angle and space-lag domain, together with the equations used to perform the mapping, show that the sample interval in the space-lag domain controls the range of angles that can be accurately recovered from the image in this domain. This is the range of angles for which the energy is well focused, at the depth of the reflector, in the angle-domain common-image gathers. From the amplitude spectrum of the lag-domain common-image gathers, we can calculate the maximum angle that limits this range. For angles greater than this upper bound, the image energy starts to spread away from the depth of the reflector. This analysis is important for the case where the angle-domain common-image gathers are employed for amplitude versus angle analysis. In this case, the amplitudes corresponding to the angles outside of this range would not be reliable, regardless of how accurate wavefield reconstruction is.

Key words: angle-decomposition, common-image gathers, extended imaging condition, wide-azimuth

1 INTRODUCTION

Many hydrocarbonate reservoirs are embedded in complex media characterized by strong velocity heterogeneity and discontinuities associated with salt bodies. In the presence of complex subsurface structures, it is crucial to form a reflector map (image) with well focused energy for efficient development and exploration of reservoirs located in such areas. The right choice of procedures, from acquisition to data processing, is of fundamental importance since they all influence the image quality.

In order to produce accurate images it is necessary that the data contain enough information about the area of interest. Even with the use of the most sophisticated processing tools and techniques, it is impossible to achieve the desired image quality from narrow-azimuth data in complex media because these data do not contain all the necessary information needed to create good images.

In the wide-azimuth acquisition context there are two relevant parameters: the azimuth of the source/receiver line (surface azimuth) and the distance between source and receiver (surface offset). The surface azimuth is the angle of the line connecting source and receiver in relation to a reference direction on the acquisition surface. In wide-azimuth acquisition the surface azimuth varies a wide range. For the rest of the paper, data from wide-azimuth survey are referred to as wide-azimuth

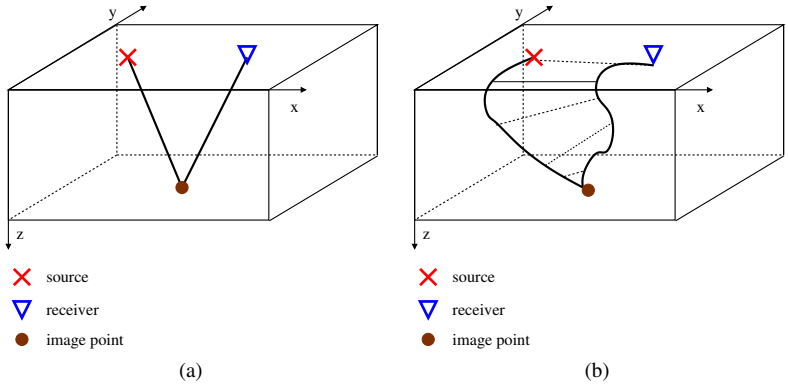

Figure 1. Schematic representations of ray paths in: simple homogeneous medium (a) and complex heterogeneous medium (b). In (a) the incident and reflected rays are straight lines whereas in (b) these rays deviate from these lines as a result of velocity variation.

data and data from narrow-azimuth surveys are referred to as narrow-azimuth data.

Data acquired at different surface azimuths illuminate different parts of the target. In complex media, where velocity varies with direction, it is desirable to illuminate each location along the reflector from many directions (at the image point) in order to study how reflectivity changes with direction. Some applications of wide-azimuth reflectivity are velocity analysis, amplitude versus angle analysis, and anisotropy estimation.

Salt bodies cause irregular illumination of targets located beneath them. This not only makes it difficult to properly image these shadow zones, but also creates spurious events in the images. Recently published work shows that it is possible to significantly improve image quality by acquiring and processing wide-azimuth data (Regone, 2006). The wide-azimuth data helps to improve resolution in velocity model (Michell *et al.*, 2006; LaDart *et al.*, 2006; Shoshitaishvili *et al.*, 2006), identify directional fractures and attenuate coherent noise (Shirui *et al.*, 2006), and consequently improve the image .

We characterize the data by two surface parameters, namely, surface offset (source/receiver offset) and surface azimuth. In general, a reflection phenomenon can be characterized by two parameters as well: reflection angle and azimuthal angle at the image point. These angles are defined locally at the image point and, in general, are not simply related to the surface parameters, as explain next.

The reflection plane is the plane containing the incident ray from the source to the reflection point, the normal to this point, and the reflected ray from the reflection point to the receiver, all measured at the image point. This plane is defined in the vicinity of the image point. The angle between the incident or reflected ray and the normal is the reflection angle. The angle that characterizes the orientation of the reflection plane, in 3D, in relation to a determined direction is the azimuthal angle A-1. When the subsurface is a homogeneous isotropic medium, the surface offset and azimuth are simply related to the reflection and azimuthal angles, respectively, at the reflection point (Figure 1(a)), independent of reflector orientation. Changes in velocity cause the incident and reflected rays to deviate from straight lines to more complicated paths (Figure 1(b)). Thus, when the medium is complex, the surface azimuth is not directly related to the azimuthal angle of the reflection plane at the image point, nor is the surface offset related to the reflection angle. Even though this relationship is not direct, a wide-azimuth acquisition is likely to increase the range of the azimuthal angles of the reflection planes at the image point.

To obtain accurate images in complex geology with large and sharp velocity variation, it is necessary to perform wavefield reconstruction using methods capable of treating lateral velocity variations, phenomena such as multipathing and finite bandwidth propagation effects (Gray *et al.*, 2001). Wavefield extrapolation by downward-continuation methods (Gazdag (1985); Gazdag & Sguazzero (1985); Stoffa *et al.* (1990); Freire & Stoffa (1986); Kessinger (1992); Cockshott & Jakubowicz (1996)), is one possible way to perform accurate wavefield reconstruction in such media, since it is capable to handle these issues. In this paper, we use the Split Step Fourier downward continuation method (Stoffa *et al.*, 1990).

Reflectivity information can be obtained by applying an imaging condition to the reconstructed source and receiver wavefields. A conventional imaging condition is a cross-correlation type imaging condition (Claerbout, 1971) that creates an image function of three-dimensional position.

Migration velocity analysis (MVA), applied after migration by downward continuation, has often been performed using lag-domain common-image gathers (Biondi *et al.*, 2003; Biondi & Symes, 2004). These gathers are usually referred to as offset-domain common-image gathers (ODCIG). However, in this paper, we use the term space-lag to refer to this domain and use the word offset for the source-receiver separation on the surface. The lag gathers can be constructed from images obtained by extended imaging conditions, that preserve the orthogonal space-lags from the source/receiver wavefield cross-correlation (Sava & Fomel, 2006). Events in the lag gathers may suffer from ambiguity on the reflection position due to multipathing, which is a common phenomenon for propagation in complex media (Nolan & Symes, 1996). Reflector position ambiguity in the lag gathers, in turn, may lead to velocity update ambiguities. To alleviate this problem,

the space-lag common-image gathers can be transformed as a function of the reflection angle at the image point. Events in angle-domain common-image gathers (ADCIG) uniquely represent energy scattered from specific locations in the subsurface. These events are uniquely associated with pairs of incident and reflected rays which, in turn, uniquely define the reflector (Prucha *et al.*, 1999; Stolk & Symes, 2002).

As indicated earlier, one way of constructing angle-dependent reflectivity is through migration by wavefield extrapolation combined with an extended imaging condition. The space-lags images can be decomposed at every image point into components that depend on the reflection angle (Sava & Fomel, 2005, 2003; Mosher & Foster, 2000; Prucha *et al.*, 1999). It is also possible to construct angle-dependent reflectivity by integral methods (Xu *et al.*, 1998; Brandsberg-Dahl *et al.*, 1999; Bleistein *et al.*, 2005). For wide-azimuth data, it is possible to decompose the space-lags in reflection and azimuthal angle (Sava & Fomel, 2003; Biondi & Tisserant, 2004; Sava & Fomel, 2005).

In this paper, we construct angle-dependent reflectivity by performing angle decomposition based on the geometry of ray vectors at the image point (Sava & Fomel, 2005). We analyze resolution in the angle-domain by means of the range of angles that can be accuratelly recovered from the space-lag domain, and of the energy focusing for reflections corresponding to these angles in the angle gathers. We can obtain the reciprocal resolution/range relationship between lag and angle-domain from the equations used to perform the lag to angle-domain mapping, together with the sampling parameters in both domains. We perform the analysis for two-dimensional (2D) and wide-azimuth three-dimensional (3D) geometries. First, this relationship shows that the sample interval in the space-lag domain controls the range of angles that can be recovered from the image in the space-lag domain. In 2D, we find that there is an angle that limits the range of reflection angles for which the energy focus, at the depth of the reflector, in the angle gathers; for angles greater than this one, the energy starts to spread. In 3D, this range varies with the azimuthal angle. Also, the range in the space-lag domain controls the sample interval in the angle-domain. Using these relationships, one can choose the parameters in both domains according to the desired resolution and range on angles for the ADCIGs. We show synthetic examples that illustrate the sampling relationship between space-lag and angle-domain as well as an example of the angle decomposition.

2 ANGLE DECOMPOSITION

Migration of seismic data consists mainly of two parts: a wavefield reconstruction procudure that creates a source wavefield U_s and a receiver (scattered) wavefield U_r, at all space locations and all times (or frequencies) given a presumed velocity field, and an imaging condition that extracts an image I (reflectivity information) from the reconstructed source and receiver wavefields, U_s and U_r.

From the reconstructed source and receiver wavefields, one can extract an image (I) by applying a conventional correlation imaging condition (Claerbout, 1971),

$$I(\mathbf{x}) = \sum_{\omega} U_r(\mathbf{x},\omega) U_s^*(\mathbf{x},\omega) \ , \tag{1}$$

where $\mathbf{x} = (x, y, z)$ are the space coordinates, ω is the temporal frequency, $U_s^*(\mathbf{x},\omega)$ is the complex conjugate of the source wavefield, $U_r(\mathbf{x},\omega)$ is the receiver wavefield, and $I(\mathbf{x})$ is the image, which depends on the particular choice of source and receiver positions. This image contains some information for velocity analysis, such as the presence of non focused diffracted energy. It is possible, however, to obtain additional velocity information, by applying a more general imaging condition, sometimes referred to as an extended imaging condition (Sava & Fomel, 2005).

One can define an extended imaging condition by space and time cross-correlation that preserves the space and/or time cross-correlation lags. Here, we employ an extended imaging condition that preserves the cross-correlation space-lags (which are, for simplicity, referred to as space-lags) to obtain an image function of the space coordinates and space-lags,

$$I(\mathbf{x},\boldsymbol{\lambda}) = \sum_{\omega} U_r(\mathbf{x}+\boldsymbol{\lambda},\omega) U_s^*(\mathbf{x}-\boldsymbol{\lambda},\omega) \ . \tag{2}$$

The image $I(\mathbf{x},\boldsymbol{\lambda})$, function of space $\mathbf{x}$ and cross-correlation space-lag, contains information for velocity analysis aimed at improving on the presumed velocity model. When the velocity model used for migration is wrong the energy does not map to the zero-lag, so we can get velocity information by looking at the energy in the image $I(\mathbf{x},\boldsymbol{\lambda})$ for the other lags different from zero. The conventional image $I(\mathbf{x})$ from equation 1 is equivalent to the extended image $I(\mathbf{x},\boldsymbol{\lambda})$ at $\boldsymbol{\lambda} = \mathbf{0}$.

An image function of space, reflection angle θ, and azimuthal angle ϕ can be obtained by mapping the information from the lag-domain into the angle-domain (Sava & Fomel, 2005)

$$I(\mathbf{x},\boldsymbol{\lambda}) \longrightarrow I(\mathbf{x},\theta,\phi) \ . \tag{3}$$

The angle between the incident or reflected ray and the reflector normal (at the image point) is the reflection angle, θ. The angle that characterizes the orientation of the reflection plane in 3D, in relation to a specified direction, is the azimuthal angle, ϕ. As mentioned earlier, these angles are related to a local geometry of source and receiver ray vectors at the image point.

The relationship between the space-lags $\boldsymbol{\lambda}$, and the reflection and azimuthal angles, θ and ϕ, in general, involves (k_x, k_y, k_z), the wavenumbers related to the space coordinates (x, y, z), and $(k_{\lambda_x}, k_{\lambda_y}, k_{\lambda_z})$, the wavenumbers related to the space-lags $(\lambda_x, \lambda_y, \lambda_z)$ (equations A-14 and A-18). It is possible to avoid the vertical space-lag λ_z by taking advantage of the fact that the wavenumber vectors $\mathbf{k_x}$ and $\mathbf{k_\lambda}$ are orthogonal (equations A-19 and A-20). This observation allows us to reduce the image $I(\mathbf{x},\boldsymbol{\lambda})$ from six to five dimensions. The mapping equations used in this work are relations A-21 and A-22 derived in the Appendix.

Implementation of equations A-21 and A-22 seemingly requires a five-dimensional Fourier transform to create AD-

CIGs, function of angles θ and ϕ, for all locations over the reflector. This transformation would involve a great computational effort and storage of a five-dimensional hypercube $I(x, y, z, \theta, \phi)$, which might not be feasible for field problems. Thus, we choose to create ADCIGs just for certain locations over the reflector, i.e., for only some x and y locations. When constructing the ADCIGs at only selected horizontal positions, we cannot apply the Fourier transform over the horizontal surface coordinates x and y, so, we cannot construct images function of space wavenumbers k_x and k_y. We can get around this limitation by considering the local slopes measured on the image at every location in space.

If we denote the local reflector dip along the x and y directions α_x and α_y, respectively, and observing that

$$\alpha_x = \frac{\partial z}{\partial x} = \frac{k_x}{k_z} \ , \tag{4}$$

and

$$\alpha_y = \frac{\partial z}{\partial y} = \frac{k_y}{k_z} \ , \tag{5}$$

we can use the dips α_x and α_y as given parameters and rewrite equations A-21 and A-22 as

$$\tan\theta = \frac{\sqrt{k_{\lambda_x}^2(1+\alpha_x^2) + k_{\lambda_y}^2(1+\alpha_y^2) + 2k_{\lambda_x}k_{\lambda_y}\alpha_x\alpha_y}}{\sqrt{k_z^2(\alpha_x^2+\alpha_y^2+1)}} \ , \tag{6}$$

and

$$\cos\phi = \frac{k_{\lambda_y}(1+\alpha_y^2) + \alpha_x\alpha_y k_{\lambda_x}}{\sqrt{m_x^2+m_y^2}} \ , \tag{7}$$

where $m_x = k_{\lambda_y}(1+\alpha_y^2) + \alpha_x\alpha_y k_{\lambda_x}$ and $m_y = k_{\lambda_x}(1+\alpha_x^2) + \alpha_x\alpha_y k_{\lambda_y}$.

In this manner, we eliminate k_x and k_y from the equations A-21 and A-22. This reduces the size of FFTs from five to three dimensions and reduces the amount of data to be stored and make computations independent for each CIG location.

Construction of one CIG by applying the angle decomposition described by relations 6 and 7 involves the following steps:

- select the horizontal CIG location (x_0, y_0) and obtain the lag-domain CIG $I(z, \lambda_x, \lambda_y) = I(x = x_0, y = y_0, z, \lambda_x, \lambda_y, \lambda_z = 0)$ from the image $I(\mathbf{x}, \boldsymbol{\lambda})$;
- apply a three-dimensional Fourier Transform on axes z, λ_x, λ_y

$$I(z, \lambda_x, \lambda_y) \rightarrow I(k_z, k_{\lambda_x}, k_{\lambda_y}) \ ; \tag{8}$$

- perform the mapping

$$I(k_z, k_{\lambda_x}, k_{\lambda_y}) \rightarrow I(k_z, \theta, \phi) \tag{9}$$

according to relations 6 and 7;
- apply a one-dimensional Inverse Fourier Transform on the depth axis

$$I(k_z, \theta, \phi) \rightarrow I(z, \theta, \phi) \ , \tag{10}$$

to obtain the angle domain CIG.

3 RESOLUTION AND RANGE IN THE ANGLE-DOMAIN

Angle-domain common-image gathers are commonly used to perform migration velocity analysis. Since these angle-domain common-image gathers are constructed from the space-lag domain common-image gathers, it is important to understand the relationship between sampling in the angle and space-lag domains. This section is devoted to analyzing angle-domain resolution and range, as a functions of the sampling parameters in the space-lag domain. The resolution study involves understanding how to choose the sampling parameters in the space-lag and angle domains such that the angle-domain be uniformly sampled and not aliased. The range analysis is meant to answer the question "What angle range can be accurately recovered for a given range and sampling in the lag-domain of migrated images obtained with extended imaging condition?" Once the relationships between angle-domain and space-lag domain sampling parameters are established, it is possible to control resolution and range in angle-domain by choosing the corresponding parameters in the space-lag domain. This analysis has implications for establishing the maximum angle range that could potentially be used for AVA and MVA.

3. 1 2D range and resolution analysis

The two-dimensional image obtained from the extended imaging condition is, in general, a function of four coordinates: $I = I(x, z, \lambda_x, \lambda_z)$. As discussed earlier, we can use geometrical relationships between the wavenumber vectors to eliminate λ_z and reduce the necessary image size from four to three dimensions, i.e., $I = I(x, z, \lambda_x)$.

Given a space-lag common-image gather $I(z, \lambda_x)$ at coordinates x, we can construct angle-domain gathers using the mapping

$$\tan\theta = \frac{k_{\lambda_x}}{k_z} \ , \tag{11}$$

which requires that the space-lag CIG be transformed to the Fourier domain.

In discussing angle-domain resolution, we consider the following parameters: origin, sample interval, and number of points on the depth axis, (o_z, d_z, n_z), and on the space lag axis, $(o_{\lambda_x}, d_{\lambda_x}, n_{\lambda_x})$; The corresponding parameters in the wavenumber-domain are: origin, sample interval, and number of points on the depth wavenumber axis, $(o_{k_z}, d_{k_z}, n_{k_z})$, and on the space-lag wavenumber axis, $(o_{k_{\lambda_x}}, d_{k_{\lambda_x}}, n_{k_{\lambda_x}})$.

Using conventional discrete Fourier transform theory, the wavenumber sampling parameters k_z and k_{λ_x} can be expressed in terms of the model parameters as

$$o_{k_z} = \frac{-1}{2d_z}, \quad d_{k_z} = \frac{1}{n_z d_z} \ , \tag{12}$$

and

$$o_{k_{\lambda_x}} = \frac{-1}{2d_{k_{\lambda_x}}}, \quad d_{k_{\lambda_x}} = \frac{1}{n_{\lambda_x} d_{\lambda_x}} \ . \tag{13}$$

The sampling parameters for the angle θ are: origin,

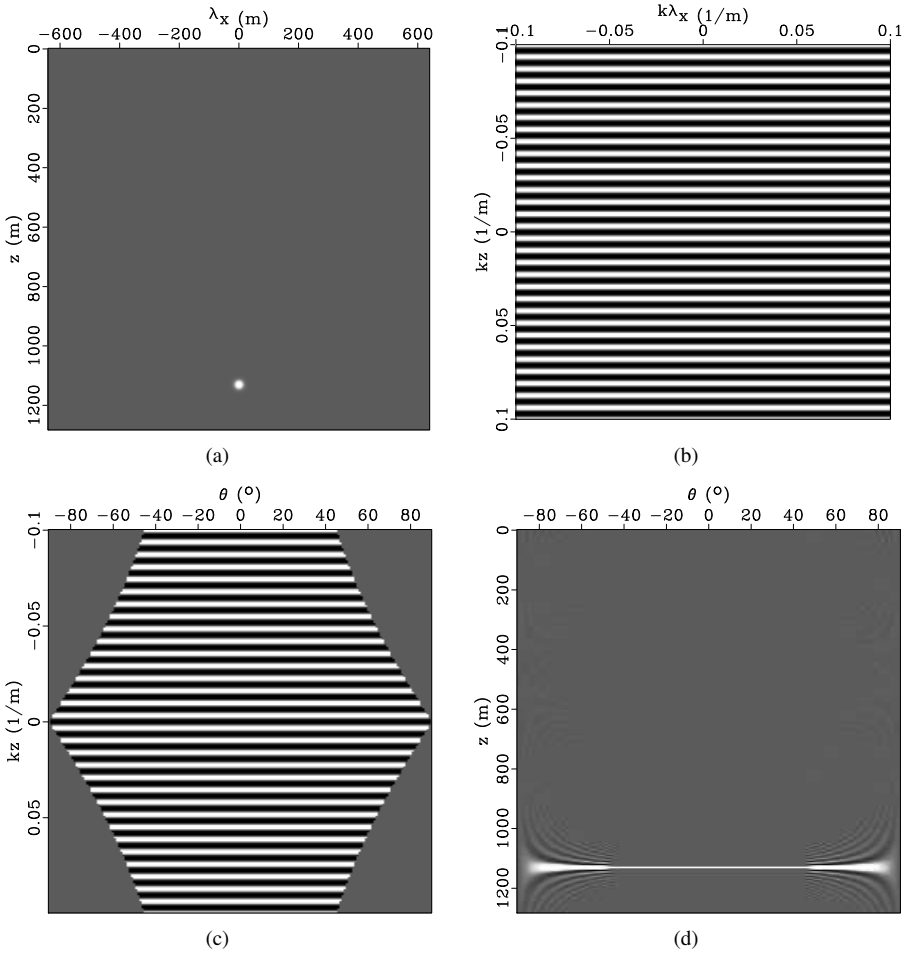

Figure 2. Example illustrating mapping from a lag gather with a single spike located at $z = 1135$ m and $\lambda_x = 0$ m: lag gather $I(z, \lambda_x)$ with one single spike (a); 2D Fourier transform $I(k_z, k_{\lambda_x})$ of the lag gather (b); mapping from k_{λ_x} to θ, $I(k_z, \theta)$ (c); angle-domain common-image gather $I(z, \theta)$ (d).

sample interval, and number of points on the depth axis, $(o_\theta, d_\theta, n_\theta)$, We can analyze the behavior of d_θ as a function of k_{λ_x}, i.e., as a function of n_{λ_x} and d_{λ_x}. Using equation 11 and the relationships 13 and 12, we have $\theta = \theta(k_z, k_{\lambda_x}) = \theta(n_z, d_z, n_{\lambda_x} d_{\lambda_x})$. Isolating θ from equation 11,

$$\theta = \arctan \frac{k_{\lambda_x}}{k_z} \ , \tag{14}$$

we can differentiate the above equation and obtain an expression for d_θ

$$d_\theta \quad = \quad \frac{k_z}{k_z^2 + k_{\lambda_x}^2} \frac{1}{n_{\lambda_x} d_{\lambda_x}} \ . \tag{15}$$

Noting that $n_{\lambda_x} d_{\lambda_x} = \lambda_{x_{max}}$, where $\lambda_{x_{max}}$ defines the range of the space-lag domain, we find

$$d_\theta = \frac{k_z}{k_z^2 + k_{\lambda_x}^2} \frac{1}{\lambda_{x_{max}}} \tag{16}$$

Thus, d_θ is inversely proportional to $n_{\lambda_x} d_{\lambda_x} = \lambda_{x_{max}}$ so the parameter λ_{max}, which is the range in space-lag domain, controls the resolution in the angle-domain: The larger the range in the space-lag domain, the better the resolution in the angle-domain.

According to equation 16, d_θ differs for each (k_z, k_{λ_x}), i.e., the angle-domain is non uniformly sampled. For processing reasons, we would like to have the angle-domain uniformly sampled. One possible way to achieve that is to sample the angle-domain uniformly using a d_θ chosen such as to avoid aliasing. The minimum value of d_θ, in order to avoid aliasing, is

$$d_{\theta_{min}} \quad = \quad \frac{k_{z_{max}}}{k_{z_{max}}^2 + k_{\lambda_{x_{max}}}^2} \frac{1}{\lambda_{x_{max}}} \tag{17}$$

$$= \quad \frac{\frac{1}{2d_z}}{\left(\frac{1}{2d_z}\right)^2 + \left(\frac{1}{2d_{\lambda_x}}\right)^2} \frac{1}{\lambda_{x_{max}}} \ . \tag{18}$$

Note that, d_θ is greater for low frequencies than for high fre-

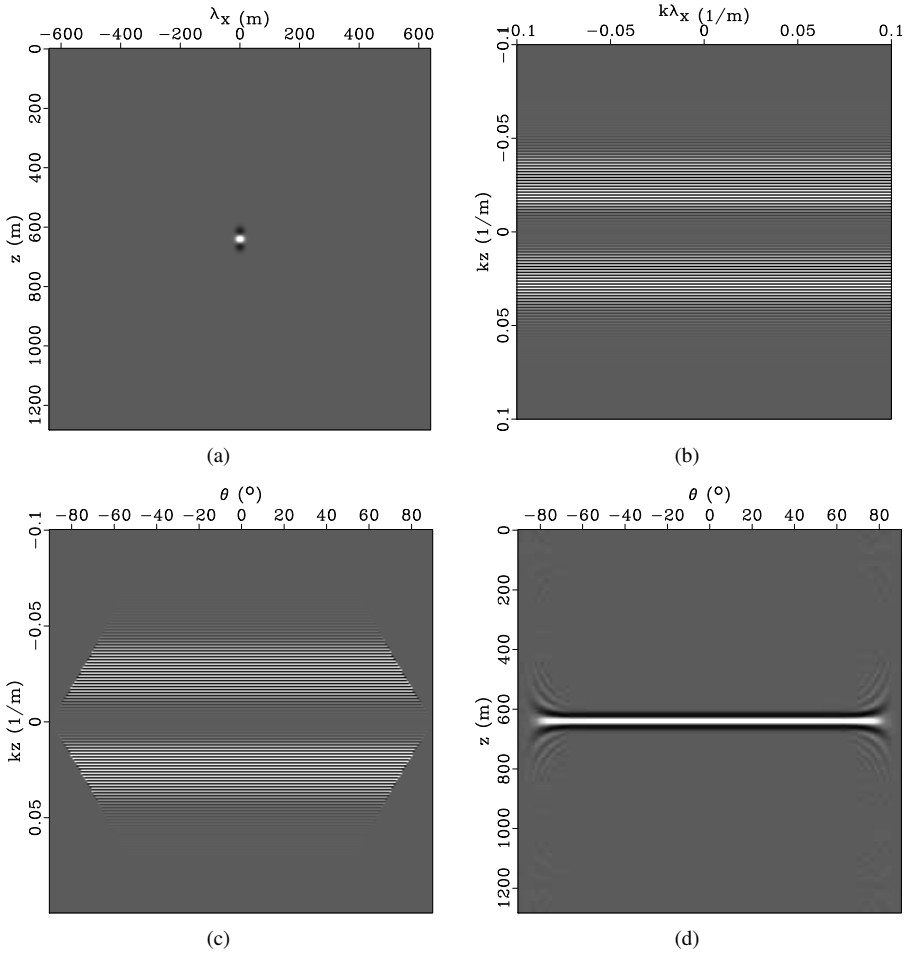

Figure 3. Example illustrating mapping from a lag gather with a wavelet located at $z = 1135$ m and $\lambda_x = 0$ m: lag gather $I(z, \lambda_x)$ with one single spike (a); 2D Fourier transform $I(k_z, k_{\lambda_x})$ of the lag gather (b); mapping from k_{λ_x} to θ, $I(k_z, \theta)$ (c); angle-domain common-image gather $I(z, \theta)$ (d).

quencies. When using $d_{\theta_{min}}$, the angles mapped from low frequencies are oversampled, because we are using a sample interval smaller than the necessary one.

Theoretically, it is possible to map events in the angle-domain CIG for all reflection angles ranging from zero (corresponding to $k_{\lambda_y} = 0$) to 90° (corresponding to $k_z = 0$). From equation 11, for each k_z, the maximum value of $\tan\theta$ mapped from k_{λ_x}, corresponds to the maximum value of this wavenumber, $k_{\lambda_{x_{max}}} = 1/(2n_{\lambda_x} d_{\lambda_x})$. As k_z increases, the maximum value of $\tan\theta$ mapped from $k_{\lambda_{x_{max}}}$ decreases and it reaches a minimum for the maximum value of the depth frequency $k_{z_{max}}$. For a band limited lag gather, $k_{z_{max}}$ is the frequency that limits the band, i.e., $k_{z_{max}}$ is the maximum k_z frequency that is different from zero. The worst scenario that would have the smaller maximum value of $\tan\theta$ would be for a wide-band lag gather, with $k_{z_{max}}$ corresponding to the Nyquist frequency, in which case $k_{z_{max}} = 1/(2n_z d_z)$. The angle corresponding to $k_{z_{max}}$ is given by

$$\begin{aligned} \theta_F &= \arctan\left(\frac{k_{\lambda_{x_{max}}}}{k_{z_{max}}}\right) \\ &= \arctan\left(\frac{1}{2d_{\lambda_x}}\frac{1}{k_{z_{max}}}\right) . \end{aligned} \tag{19}$$

Thus, not only $k_{z_{max}}$ but also the sample interval in the λ_x dimension, controls θ_F. The angle θ_F defines the range of angles that can be accurately recovered from the lag-domain. For reflection angles greater than θ_F, we observe energy defocusing and spreading away from the depth of the reflector. This phenomenon becomes more pronounced for increasing angles. Therefore, even if there is information in the lag gather corresponding to reflection at 90° in the angle gather, when mapped to the angle-domain, the energy corresponding to this event is defocused as discussed next.

In order to analyze and visualize this transformation from lag to angle-domain, we consider the idealized case of a lag gather that consists of a spike at depth $z = 1135$ m. Ide-

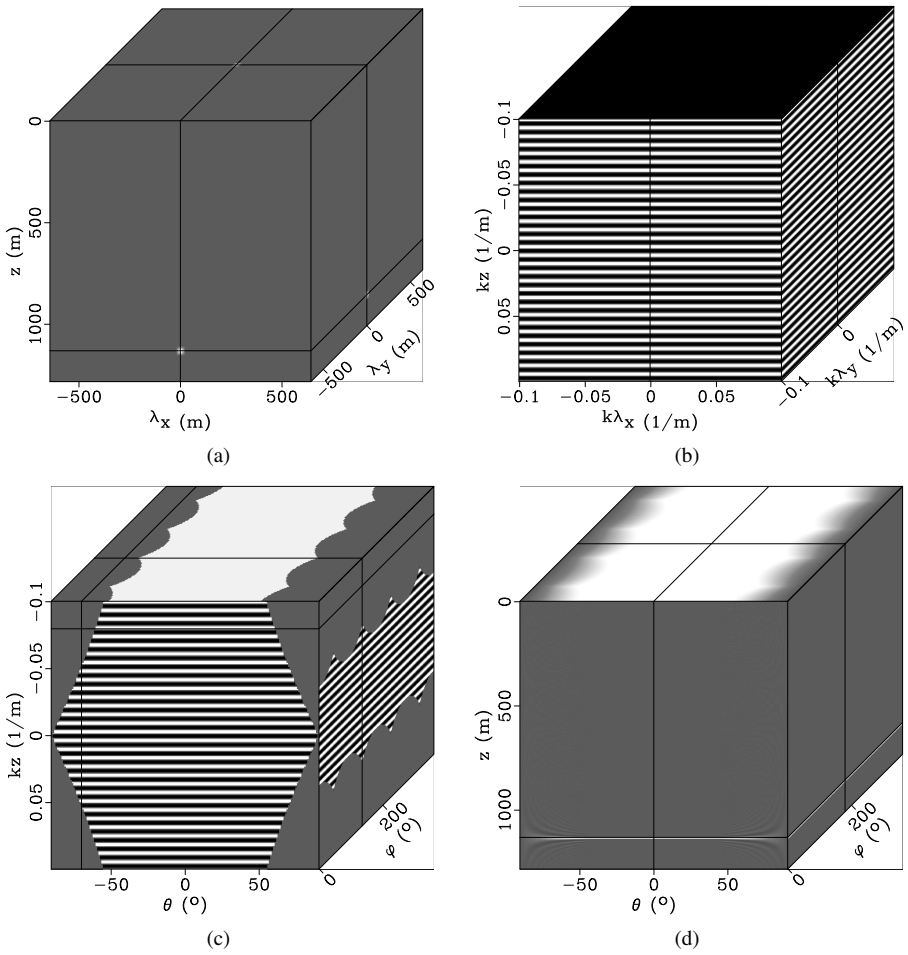

Figure 4. Example illustrating mapping from a 3D lag gather with a single spike located at $z = 1135$ m and $\lambda_x = \lambda_y = 0$ m: lag gather $I(z, \lambda_x, \lambda_y)$ with one single spike (a); 2D Fourier transform of the lag gather $I(k_z, k_{\lambda_x}, k_{\lambda_y})$ (b); mapping from $(k_{\lambda_x}, k_{\lambda_y})$ to (θ, ϕ), $I(k_z, \theta, \phi)$ (c); angle-domain common-image gather $I(z, \theta, \phi)$ (d).

ally, the angle-domain common-image gather obtained from this space-lag domain gather should contain reflections for the whole range of θ, from zero to 90°.

The example in Figures 2(a) – 2(d) illustrates the relationships between angle and space-lag domain parameters, as discussed in the preceding section. Figure 2(a) represents the synthetic lag gather $I(z, \lambda_x)$ with one single spike located at $z = 1135$ and $\lambda_x = 0$ m. Figure 2(b) is the 2D Fourier transform $I(k_z, k_{\lambda_x})$ of the lag gather. Figure 2(c) shows the result after applying the mapping $k_{\lambda_x} \rightarrow \theta$, according to relation 11, to obtain $I(k_z, \theta)$. As discussed earlier, as k_z increases, the mapping from equation 11 leads to a decreasing range of $\tan\theta$ for each fixed value of k_z, which in turn leads to decreasing values of θ. The angle gather $I(z, \theta)$ is shown on Figure 2(d). In this example, $d_z = d_{\lambda_x} = 5$ m so, $\theta_F = 45^\circ$. Up to angle θ_F, the energy is well focused at the true depth of the reflector, and after this point is starts to defocus. In $I(k_z, \theta)$, Figure 2(c), up to the value $\tan\theta_F = 45$, information exists at all values of k_z and beyond that there is a decrease in information associated with higher absolute values of k_z. One can think of the data in $I(k_z, \theta)$ as the data from $I(k_z, k_{\lambda_x})$ multiplied by a boxcar filter of different width for each k_{λ_x}. Therefore, after applying the inverse Fourier transform on the axis k_z to obtain $I(z, \theta)$, the angles corresponding the the boxcar filtered data appear convolved with a sinc function, and the energy corresponding to these angles defocuses, spreading away from the depth of the reflector, as seen in Figure 2(d). Thus, the analysis of angle-domain range involves finding θ_F which is the maximum angle of energy that is well focused at the reflector depth. The relevance of calculating θ_F is that if one wants to use ADCIGs to perform amplitude analysis, the amplitudes for angles greater than θ_F would not be reliable because of the energy spreading effect caused by the angle-mapping transformations.

Figures 3(a) – 3(d) are similar to Figures 2(a) – 2(d). All subplots have the same meaning as the ones in the previous example. Since the lag gather image is band-limited, it does not contain the zero depth wavenumber $k_z = 0$, therefore, for this

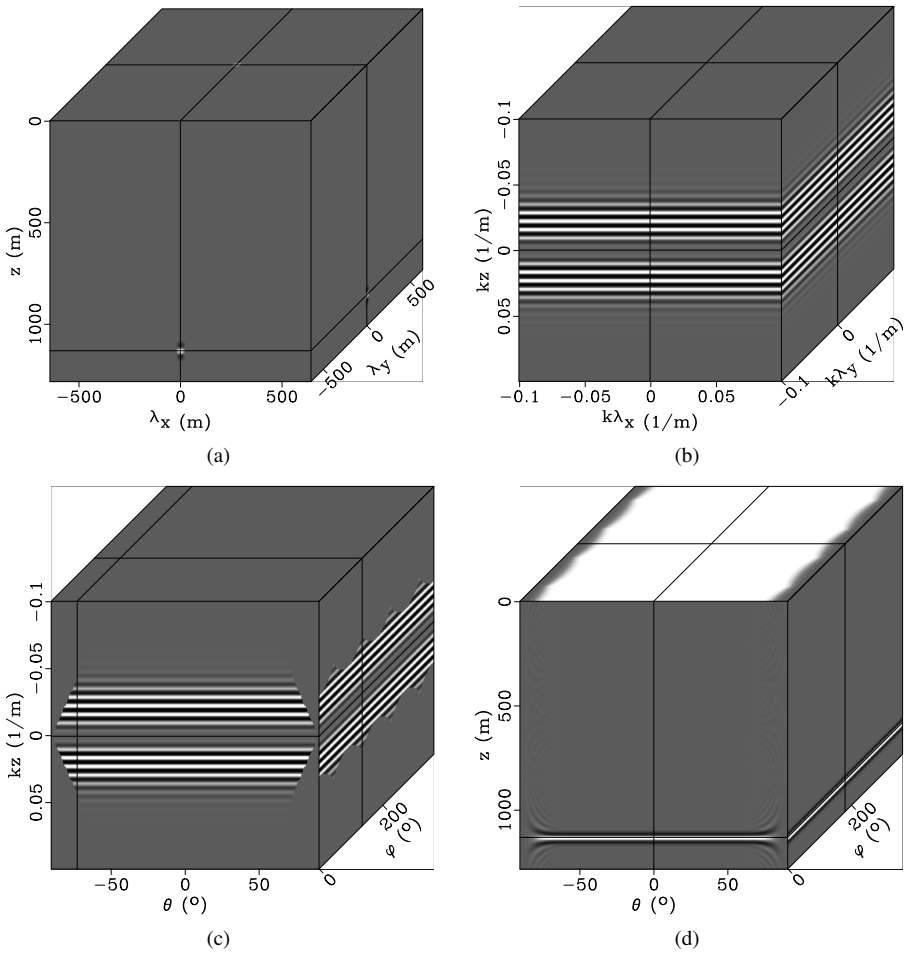

Figure 5. Example illustrating mapping from a 3D lag gather with a wavelet located at $z = 1135$ m and $\lambda_x = \lambda_y = 0$ m: lag gather $I(z, \lambda_x, \lambda_y)$ with one single spike (a); 2D Fourier transform of the lag gather $I(k_z, k_{\lambda_x}, k_{\lambda_y})$ (b); mapping from $(k_{\lambda_x}, k_{\lambda_y})$ to (θ, ϕ), $I(k_z, \theta, \phi)$ (c); angle-domain common-image gather $I(z, \theta, \phi)$ (d).

more realistic example, there are no reflections corresponding to angles up to 90°. The highest depth wavenumber is about 0.05 and the maximum lag wavenumber is 0.1, leading to θ_F about 63°, Figure 3(d).

From the examples in Figures 2(a) – 2(d) and Figures 3(a) – 3(d), the reflection energy is not well focused at the reflector depth for the angles greater than θ_F. This angle, is the ratio between the maximum lag wavenumber and maximum depth wavenumber in the lag gather. In the first example we do not have events corresponding to up to 90° in the angle gather because of the energy defocusing that occurs for angles after θ_F. For the second example, the angle gather do not have energy at up to 90° because there is no information at $k_z = 0$, in addition to the deforming phenomenon caused by band limiting the depth wavenumber spectrum over the angle θ_F.

3. 2 3D range and resolution analysis

A similar analysis to the one performed in the preceding section can be done for the more general 3D case. Here, we limit our analysis to the case of a horizontal reflector. In this case, we are discussing about wide-azimuth angle-decomposition so, there are two angles for which we need to perform the range and resolution analysis: the reflection angle θ and the azimuthal angle ϕ.

A 3D lag-domain common-image gather can be described as function of two space-lags: λ_x and λ_y. The additional 3D model parameters are: origin, sample interval and number of points on the space-lag axis λ_y, $(o_{\lambda_y}, d_{\lambda_y}, n_{\lambda_y})$, on the wavenumber axis k_{λ_y}, $(o_{k_{\lambda_y}}, d_{k_{\lambda_y}}, n_{k_{\lambda_y}})$, and on the azimuthal angle axis ϕ, (o_ϕ, d_ϕ, n_ϕ).

For a 3D horizontal reflector, the reflection angle θ can be computed using the relation

$$\tan\theta = \frac{\sqrt{k_{\lambda_x}^2 + k_{\lambda_y}^2}}{k_z} \;, \tag{20}$$

and the azimuthal angle ϕ can be computed using the relations

$$\cos\phi = \frac{k_{\lambda_y}}{\sqrt{k_{\lambda_x}^2 + k_{\lambda_y}^2}} \ . \tag{21}$$

Similarly to the 2D case, we can analyze the behavior of d_θ and d_ϕ as functions of k_{λ_x} and k_{λ_y}, i.e., as a function of n_{λ_x} and d_{λ_x}, and n_{λ_y} and d_{λ_y}. We rewrite equations 20 and 21 as

$$\theta = \arctan\frac{\sqrt{k_{\lambda_x}^2 + k_{\lambda_y}^2}}{k_z} \ , \tag{22}$$

and

$$\phi = \arccos\frac{k_{\lambda_y}}{\sqrt{k_{\lambda_x}^2 + k_{\lambda_y}^2}} \ , \tag{23}$$

To study how d_θ changes with k_{λ_x} and k_{λ_y}, we differentiate equation 22 first with respect to k_{λ_x}

$$d_\theta = \frac{k_z k_{\lambda_x}}{(k_z^2 + k_{\lambda_x}^2 + k_{\lambda_y}^2)\sqrt{k_{\lambda_x}^2 + k_{\lambda_y}^2}} \frac{1}{n_{\lambda_x} d_{\lambda_x}} \ , \tag{24}$$

and then with respect to k_{λ_y}

$$d_\theta = \frac{k_z k_{\lambda_y}}{(k_z^2 + k_{\lambda_x}^2 + k_{\lambda_y}^2)\sqrt{k_{\lambda_x}^2 + k_{\lambda_y}^2}} \frac{1}{n_{\lambda_y} d_{\lambda_y}} \ . \tag{25}$$

Similarly, to study how d_ϕ changes with k_{λ_x} and k_{λ_y}, we differentiate equation 23 first with respect to k_{λ_x}

$$d_\phi = \frac{1}{\sqrt{1 + \frac{k_{\lambda_y}^2}{k_{\lambda_x}^2 + k_{\lambda_y}^2}}} \frac{-k_{\lambda_x} k_{\lambda_y}}{(k_{\lambda_x}^2 + k_{\lambda_y}^2)^{3/2}} \frac{1}{n_{\lambda_x} d_{\lambda_x}} \tag{26}$$

and then with respect to k_{λ_y}

$$d_\phi = \frac{1}{\sqrt{1 + \frac{k_{\lambda_y}^2}{k_{\lambda_x}^2 + k_{\lambda_y}^2}}} \frac{k_{\lambda_x}^2}{(k_{\lambda_x}^2 + k_{\lambda_y}^2)^{3/2}} \frac{1}{n_{\lambda_y} d_{\lambda_y}} \tag{27}$$

Equations 24, 25, 26, and 27 show that d_θ and d_ϕ are both inversely proportional to $n_{\lambda_x} d_{\lambda_x} = \lambda_{x_{max}}$ and $n_{\lambda_y} d_{\lambda_y} = \lambda_{y_{max}}$, where the parameters $\lambda_{x_{max}}$ and $\lambda_{y_{max}}$ are the ranges in space-lag domain, which control the resolution in the angle-domain. As in the preceding section, we conclude that the larger the range in the space-lag domain, the better the resolution in the angle-domain.

Using similar arguments to the ones employed for the 2D analysis, to uniformly sample the angle-domain and avoiding aliasing, the parameters d_θ and d_ϕ need to be lesser or equal to their minimum possible values given by substituting the wavenumbers in equations 24, 25, 26,and 27 by their maximum values (Nyquist). This way, there are two possible values for both d_θ and d_ϕ, and the minimum of the two should be used in each case.

From equation 22, for each k_{λ_y} there is an angle that can be mapped from the lag-domain, given by $k_{\lambda_{x_{max}}}$ and $k_{z_{max}}$ (as defined in previous section), that limits the range of angles for which there is information at all values of k_z. We define θ_F in 3D as the smallest of these angles, which corresponds to $k_{\lambda_y} = 0$ in equation 22. This angle θ_F defines the range of reflection angles that can be accurately recovered from the lag-domain, because this range of angles contains information for all depth wavenumbers k_z for all azimuths. The maximum θ for which there is information at all wavenumbers k_z changes with ϕ. Outside the range defined by θ_F, due to the fact that this maximum θ changes with ϕ, there are an uneven information distribution along the ϕ dimension, with respect to k_z. The azimuthal angles 45, 135, 225, and 315° have more information at more wavenumbers k_z than the other angles, and there is a decrease on this wavenumbers as angles goes away from these four ones, reaching a minimum at 0, 90, 180, and 270°. Thus, reflections occuring at these four azimuthal angles where there is more information, or in their vicinity, have better focused events in the angle gathers than at other azimuthal angles.

Similarly to the 2D case, we construct synthetic 3D lag-gathers (first with a spike and then with a band-limited wavelet at zero lag in x and y) and study the steps envolved in the implementation of the mappings described in equations 20 and 21.

For the first example, we construct a lag gather $I(z, \lambda_x, \lambda_y)$ with a spike at $(z = 1135, \lambda_x = 0, \lambda_y = 0)$. Then, we apply a 3D Fourier transform on the lag gather to obtain $I(k_z, k_{\lambda_x}, k_{\lambda_y})$. Next, we apply the mappings in equations 20 and 21 to get $I(k_z, \theta, \phi)$. And, finally, we inverse Fourier transform the axis k_z to create the angle gather $I(z, \theta, \phi)$. Figures 4(a) to 4(d) shows four 3D plots representing the image in these four domains. In each of the 3D plots, the cross lines show the position of the sections displayed on the surfaces. Figure 4(a) is the lag gather, $I(z, \lambda_x, \lambda_y)$, with one single spike. Figure 4(b) is the 3D Fourier transform, $I(k_z, k_{\lambda_x}, k_{\lambda_y})$, of the lag gather. Figure 4(c) shows both mappings from equations 20 and 21 applied to $I(k_z, k_{\lambda_x}, k_{\lambda_y})$ to obtain $I(k_z, \theta, \phi)$. For this wide-band example $\theta_F = 45$ because the lag gather has information for all wavenumbers (wide-band) and the sample interval in all dimensions are equal. In the (k_z, θ) cross-section in Figure 4(c), for angles θ up to 45° information exists at all wavenumbers k_z, and for angles greater than 45° there is an uneven information distribution along the ϕ dimension, with respect to k_z. The azimuthal angles 45, 135, 225, and 315° have more information at more wavenumbers k_z than the other angles, and there is a decrease on this wavenumbers as angles goes away from these four ones, reaching a minimum at 0, 90, 180, and 360°. The same pattern can be been in the (k_z, ϕ) cross-section in this same Figure. For the reflection angles in the interval $|\theta| <= 45$, the energy is well focused in the angle gathers for all azimuthal angles.

As in the 2D case, for the next example, we construct a 3D lag gather with a wavelet rather than a spike, with the intent of simulating a more realistic situation (a band-limited lag-gather). Figures 5(a) – 5(d) shows, respectively, $I(z, \lambda_x, \lambda_y)$, $I(k_z, k_{\lambda_x}, k_{\lambda_y})$, $I(k_z, \theta, \phi)$, $I(z, \theta, \phi)$. The wavelet in the 3D lag gather is band limited and the maximum depth wavenum-

ber is smaller than the Nyquist frequency $k_{z_{max}}$. That causes the angle θ_F for this case to be greater than for the previous example. Therefore, in this case, the range of angles for which the energy is well focused in the 3D angle-domain common-image gather, for all azimuthal angles, is larger than for the spike lag example (around 63°). As for the preceding example, the angle θ_F changes with azimuth reaching maximum values at $\phi = 45$, 135, 225, and 315°.

4 EXAMPLES

The following two examples are meant to illustrate the relationships discussed in preceding section. We create two examples with equal geometry but different velocity models. In both examples the velocity varies with depth, $v = v(z)$, but with negative and positive gradients, respectively. We construct CIGs for the same locations in both cases, as illustrated in Figure 6. For the first example, the reflection angles for these CIG locations are within the range of well focused energy discussed in the previous section, i.e., the reflection angles at these locations are smaller than θ_F for each gather. In this case, the energy in the angle gathers are well focused. In the second example, the reflection angles in all gathers but one are greater than θ_F, and in this case the energy is less well focused.

The reflectivity model is a horizontal reflector embedded in a $v = v(z)$ medium. The model parameters are: $(o_x, d_x, n_x) = (0, 30, 180)$, $(o_y, d_y, n_y) = (0, 30, 180)$, and $(o_z, d_z, n_z) = (0, 5, 180)$. There is one source located in the center of the horizontal plane. The reflector is located at depth $z = 700$ m. The velocity model for the first example is $v(z) = 4500 - 4z$. The synthetic data (due to one source) $D(x, y, t)$ and migrated image $I(\mathbf{x})$ is shown in Figure 7. There, we can see the flat reflector located at depth $z_r = 700$m.

As discussed earlier, we construct ADCIGs just for some locations over the reflector. From the hypercube image $I(\mathbf{x}, \boldsymbol{\lambda})$ we can select a location in the horizontal space, $(x, y) = (x_0, y_0)$, where we want to construct a ADCIG, and obtain the three-dimensional subset $I_h = I(x = x_0, y = y_0, z, \lambda_x, \lambda_y, \lambda_z = 0)$. Figure 8 shows lag gathers for nine different locations at the reflector depth (Figure 6). Each gather is obtained by selecting the depth of the reflector, thus, each gather represents the set $I_h = I(x = x_0, y = y_0, z = z_r, \lambda_x, \lambda_y, \lambda_z = 0)$. The gather in the center has the same horizontal location as the source. The gathers around the central one are located 300 m away from it in one or both horizontal directions. For each panel in Figure 8, the horizontal axis is λ_x and the vertical is λ_y.

We create an angle gather for each lag gather. To better visualize an ADCIG, we make use of polar plots. Figure 9 helps in locating and understanding how an event appears on a polar plot. The azimuthal angle ϕ is zero at the positive horizontal direction and increases in the counter-clockwise direction. The distance from the center of the circles to the event represents the angle θ, which has a minimum value of zero for events appearing in the center of the Figure, and a maximum value of 90 for events locateded on the outer circle. The angle gathers obtained from the lag gathers in Figure 8 are shown in Figure 10.

As the medium is homogeneous and the reflector is horizontal, the azimuth of the reflection plane coincides with the source-receiver azimuth on the surface. As can be seen in Figure 10, the azimuth of the reflection planes coincides with the azimuth of the source-receiver direction. The central polar plot corresponds to the image point right under the source and, as expected, we have an event at $\theta = 0$, i.e., we have normal incidence at this point. We can see in these gathers that the energy is very focused, as expected, since the reflection angles are within the complete energy focusing range.

The velocity model for the second example is $v(z) = 1000 + 4z$. The synthetic data $D(x, y, t)$ and migrated image $I(\mathbf{x})$ is shown in Figure 11. There, we can see the flat reflector located at depth $z_r = 700$m.

Figure 12 shows nine lag gathers for the same nine locations in the previous example. Each gather is also obtained by selecting the depth of the reflector in $I_h = I(x = x_0, y = y_0, z = z_r, \lambda_x, \lambda_y, \lambda_z = 0)$. The angle gathers obtained from the lag gathers in Figure 12 are shown in Figure 13.

As can be seen in Figure 13 the energy is less well focused compared to Figure 10. That is because the reflection angles are outside the range of well focused energy defined by the angle θ_F explained in the preceding sections. The central CIG looks defocused even though the reflection angle is zero at this location. This is due to a low clip value used to create the plots in that case. We could see through these two examples how the energy focuses well or not depending on whether the reflection angles are inside or outside the range of complete energy focusing. The angles θ and ϕ in the images are validated by theoretical expressions found in Dobrin (1988).

5 CONCLUSIONS

One can extract angle information from the image $I(\mathbf{x}, \boldsymbol{\lambda})$ just by using simple relationships between the ray parameters vectors. Using this angle information we can construct angle dependent reflectivity. The model parameters control the range of reflection angles that can be recovered from the image with well focused events in the angle-domain common-image gathers. In general, the angle that limits this range is proportional to the ratio between maximum depth wavenumber and maximum space-lag wavenumber. It may not be possible to change the sample intervals in the lag-domain because this is usually the same as the ones in characterizing the space-domain coordinates. Conventional implementations of extended imaging condition keep the space and space-lag samplings the same. The largest wavenumbers of the lag gather limit the range of angles for which one can "trust" the amplitudes in the angle gather. This is particularly important if these angle gathers are being employed to perform amplitude versus angle analysis or migration velocity analysis.

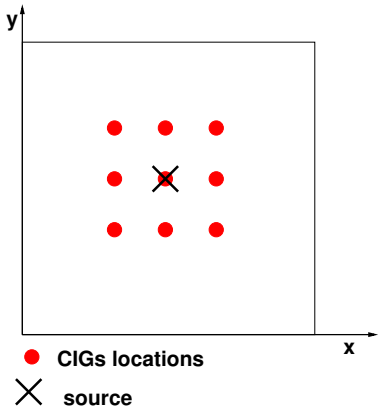

Figure 6. CIG locations. Each circle is a CIG location and the cross is the source location. The central CIG horizontal location is the same as the source location. The CIGs around the central one are 300 meters apart in both x and y directions.

REFERENCES

Biondi, B., and Symes, W., 2004, Angle-domain common-image gathers for migration velocity analysis by wavefield-continuation imaging: Geophysics, **69**, no. 5, 1283–1298.

Biondi, B., and Tisserant, T., 2004, 3D angle-domain common-image gathers for migration velocity analysis: Geophys. Prosp., **52**, no. 6, 575–591.

Biondi, B., Tisserant, T., and Symes, W., 2003, Wavefield-continuation angle-domain common-image gathers for migration velocity analysis: Wavefield-continuation angle-domain common-image gathers for migration velocity analysis:, Soc. of Expl. Geophys., 73rd Ann. Internat. Mtg., 2104–2107.

Bleistein, N., Zhang, Y., Xu, S., Zhang, G., and Gray, S. H., 2005, Kirchhoff inversion in image point coordinates recast as source/receiver point processing: SEG Technical Program Expanded Abstracts, , no. 1, 1697–1700.

Brandsberg-Dahl, S., de Hoop, M. V., and Ursin, B., 1999, The sensitivity transform in the common scattering-angle/azimuth domain: The sensitivity transform in the common scattering-angle/azimuth domain:, Eur. Assn. Geosci. Eng., 61st Mtg., Session:4053.

Claerbout, J. F., 1971, Toward a unified theory of reflector mapping: Geophysics, **36**, no. 03, 467–481.

Cockshott, I., and Jakubowicz, H., 1996, 3D migration using the Fourier finite difference method: 3D migration using the Fourier finite difference method:, Eur. Assn. Geosci. Eng., 58th Mtg., Session:P093.

Dobrin, M. B., 1988, Introduction to geophysical prospecting: , McGraw-Hill Book Co., 4th ed. edition.

Freire, R., and Stoffa, P. L., 1986, Migration using the 'Split-step Fourier' method: Migration using the 'Split-step Fourier' method:, Soc. of Expl. Geophys., 56th Ann. Internat. Mtg., Session:POS2.1.

Gazdag, J., and Sguazzero, P., 1985, Migration of seismic data by phase shift plus interpolation *in* Gardner, G. H. F., Ed., Migration of seismic data:: Soc. of Expl. Geophys., 323–330.

Gazdag, J., 1985, Wave equation migration with the phase-shift method *in* Gardner, G. H. F., Ed., Migration of seismic data:: Soc. of Expl. Geophys., 302–311.

Gray, S. H., Etgen, J., Dellinger, J., and Whitmore, D., 2001, Seismic migration problems and solutions: Geophysics, **66**, no. 5, 1622–1640.

Kessinger, W., 1992, Extended split-step Fourier migration: Extended split-step Fourier migration:, Soc. of Expl. Geophys., 62nd Ann. Internat. Mtg, 917–920.

LaDart, S., Lee, J., Shoshitaishvili, E., Etgen, J., and Michell, S., 2006, Wide azimuth tomography - is it necessary?: Wide azimuth tomography - is it necessary?:, Soc. of Expl. Geophys.

Michell, S., Shoshitaishvili, E., Chergotis, D., Sharp, J., and Etgen, J., 2006, Wide azimuth streamer imaging of Mad Dog; Have we solved the subsalt imaging problem?: Wide azimuth streamer imaging of Mad Dog; Have we solved the subsalt imaging problem?:, Soc. of Expl. Geophys.

Mosher, C., and Foster, D., 2000, Common angle imaging conditions for prestack depth migration: Common angle imaging conditions for prestack depth migration:, Soc. of Expl. Geophys., 70th Ann. Internat. Mtg, 830–833.

Nolan, C. J., and Symes, W. W., 1996, Imaging and coherency in complex structures: Imaging and coherency in complex structures:, Soc. of Expl. Geophys., 66th Ann. Internat. Mtg, 359–362.

Prucha, M., Biondi, B., and Symes, W., 1999, Angle-domain common image gathers by wave-equation migration: Angle-domain common image gathers by wave-equation migration:, Soc. of Expl. Geophys., 69th Ann. Internat. Mtg, 824–827.

Regone, C. J., 2006, A modeling approach to wide-azimuth design for subsalt imaging: The Leading Edge, **25**, no. 12, 1467–1475.

Sava, P. C., and Fomel, S., 2003, Angle-domain common-image gathers by wavefield continuation methods: Geophysics, **68**, no. 3, 1065–1074.

Sava, P., and Fomel, S., 2005, Coordinate-independent angle-gathers for wave equation migration: SEG Technical Pro-

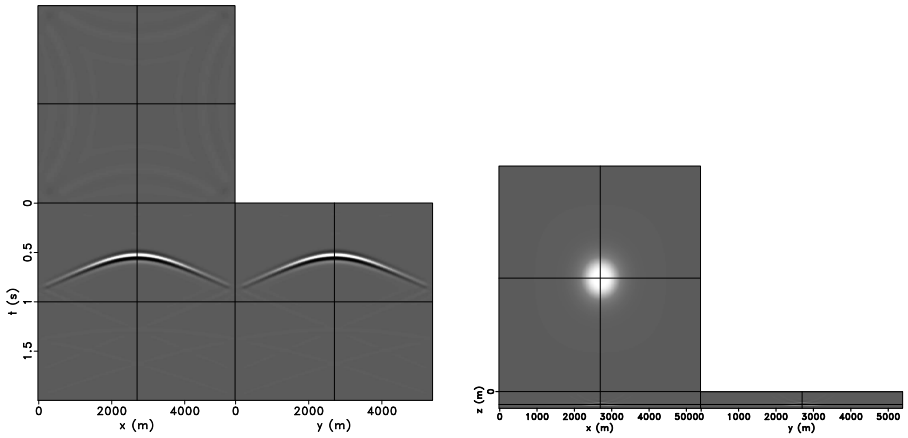

(a) (b)

Figure 7. Data for the one shot located at center of x-axis (a), and image of horizontal reflector located at $z_r = 700$ m (b).

gram Expanded Abstracts, , no. 1, 2052–2055.

Sava, P., and Fomel, S., 2006, Time-shift imaging condition in seismic migration: Geophysics, **71**, no. 6, S209–S217.

Shirui, W., Yun, L., and Xiangyu, G., 2006, Application of wide azimuth land 3D - a case history.: Application of wide azimuth land 3D - a case history.:, Soc. of Expl. Geophys.

Shoshitaishvili, E., Michell, S., Etgen, J., Chergotis, D., and Olson, E., 2006, Improving resolution of top salt complexities for subsalt imaging.: Improving resolution of top salt complexities for subsalt imaging.:, Soc. of Expl. Geophys.

Stoffa, P. L., Fokkema, J. T., de Luna Freire, R. M., and Kessinger, W. P., 1990, Split-step Fourier migration: Geophysics, **55**, no. 04, 410–421.

Stolk, C. C., and Symes, W., 2002, Artifacts in Kirchhoff common image gathers: Artifacts in Kirchhoff common image gathers:, Soc. of Expl. Geophys., 72nd Ann. Internat. Mtg, 1129–1132.

Xu, S., Chauris, H., Lambare, G., and Noble, M. S., 1998, Common angle image gather: A new strategy for imaging complex media: Common angle image gather: A new strategy for imaging complex media:, Soc. of Expl. Geophys., 68th Ann. Internat. Mtg, 1538–1541.

6 APPENDIX - ANGLE DECOMPOSITION EQUATIONS

This appendix closely follows the derivation from Sava & Fomel (2005).

The image obtained from the space-lag (extended) imaging condition (equation2) is function of space $\mathbf{x}$ and space-lags $\boldsymbol{\lambda}$. We can define the local source and receiver coordinates $\mathbf{s} = (s_x, s_y, s_z)$ and $\mathbf{r} = (r_x, r_y, r_z)$, respectively, in terms of $\mathbf{x}$ and $\boldsymbol{\lambda}$ (Figure A-1),

$$\mathbf{s} = \mathbf{x} - \boldsymbol{\lambda} \,, \tag{A-1}$$

$$\mathbf{r} = \mathbf{x} + \boldsymbol{\lambda} \,. \tag{A-2}$$

The two-way traveltime $t = t(\mathbf{x}, \boldsymbol{\lambda})$ from a source to a receiver location is a function of $\mathbf{x}$ and $\boldsymbol{\lambda}$. The traveltime can be regarded as function of $\mathbf{s}$ and $\mathbf{r}$, $t = t\left(\frac{\mathbf{r}+\mathbf{s}}{2}, \frac{\mathbf{r}-\mathbf{s}}{2}\right)$. Changes in the traveltime with respect to change in x, y and z are, respectively,

$$\begin{aligned} \frac{\partial t}{\partial x} &= \frac{\partial t}{\partial r_x}\frac{\partial r_x}{\partial x} + \frac{\partial t}{\partial s_x}\frac{\partial s_x}{\partial x} \\ &= \frac{\partial t}{\partial r_x} + \frac{\partial t}{\partial s_x} \,, \end{aligned} \tag{A-3}$$

and

$$\begin{aligned} \frac{\partial t}{\partial y} &= \frac{\partial t}{\partial r_y}\frac{\partial r_y}{\partial y} + \frac{\partial t}{\partial s_y}\frac{\partial s_y}{\partial y} \\ &= \frac{\partial t}{\partial r_y} + \frac{\partial t}{\partial s_y} \,, \end{aligned} \tag{A-4}$$

and

$$\begin{aligned} \frac{\partial t}{\partial z} &= \frac{\partial t}{\partial r_z}\frac{\partial r_z}{\partial z} + \frac{\partial t}{\partial s_z}\frac{\partial s_z}{\partial z} \\ &= \frac{\partial t}{\partial r_z} + \frac{\partial t}{\partial s_z} \,, \end{aligned} \tag{A-5}$$

Similarly, changes in the traveltime with respect to λ_x, λ_y and λ_z are, respectively,

$$\begin{aligned} \frac{\partial t}{\partial \lambda_x} &= \frac{\partial t}{\partial r_x}\frac{\partial r_x}{\partial \lambda_x} + \frac{\partial t}{\partial s_x}\frac{\partial s_x}{\partial \lambda_x} \\ &= \frac{\partial t}{\partial r_x} - \frac{\partial t}{\partial s_x} \,. \end{aligned} \tag{A-6}$$

and

$$\begin{aligned} \frac{\partial t}{\partial \lambda_y} &= \frac{\partial t}{\partial r_y}\frac{\partial r_y}{\partial \lambda_y} + \frac{\partial t}{\partial s_y}\frac{\partial s_y}{\partial \lambda_y} \\ &= \frac{\partial t}{\partial r_y} - \frac{\partial t}{\partial s_y} \,, \end{aligned} \tag{A-7}$$

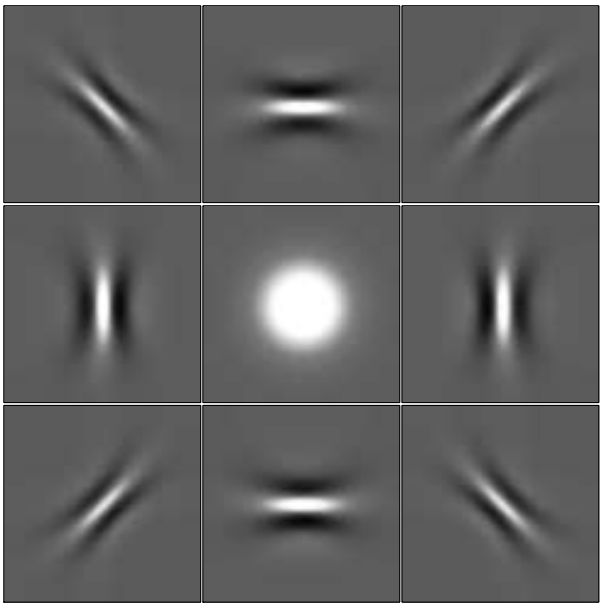

Figure 8. Space-lag domain common-image gathers: each individual plot is a lag gather for a different horizontal location over the reflector. In each Figure, the horizontal axis is λ_x and the vertical is λ_y. The gather in the center has the same horizontal location as the source. The gathers around the central one are located 300 m away from it in one or both horizontal directions.

and

$$\begin{aligned}\frac{\partial t}{\partial \lambda_z} &= \frac{\partial t}{\partial r_z}\frac{\partial r_z}{\partial \lambda_z} + \frac{\partial t}{\partial s_z}\frac{\partial s_z}{\partial \lambda_z} \\ &= \frac{\partial t}{\partial r_z} - \frac{\partial t}{\partial s_z}\,, \end{aligned} \tag{A-8}$$

Since $\mathbf{p} = \nabla t$, we can relate the wavenumber vectors as

$$\mathbf{p}\boldsymbol{x} = \mathbf{p}\boldsymbol{r} + \mathbf{p}\boldsymbol{s}\,, \tag{A-9}$$

$$\mathbf{p}_{\boldsymbol{\lambda}} = \mathbf{p}\boldsymbol{r} - \mathbf{p}\boldsymbol{s}\,. \tag{A-10}$$

where $\mathbf{p}\boldsymbol{x}$, $\mathbf{p}_{\boldsymbol{\lambda}}$, $\mathbf{p}\boldsymbol{s}$, and $\mathbf{p}\boldsymbol{r}$ are the wavenumber vectors relative to $\mathbf{x}$, $\boldsymbol{\lambda}$, $\mathbf{s}$, and $\mathbf{r}$, respectively.

If $\mathbf{k}\boldsymbol{x}$ and $\mathbf{k}_{\boldsymbol{\lambda}}$ are the space and space-lag wavenumber vectors, respectively, we have

$$\mathbf{p}\boldsymbol{x} = \frac{\mathbf{k}\boldsymbol{x}}{\omega}\,, \tag{A-11}$$

$$\mathbf{p}_{\boldsymbol{\lambda}} = \frac{\mathbf{k}_{\boldsymbol{\lambda}}}{\omega}\,. \tag{A-12}$$

Using the fact that $\mathbf{p}\boldsymbol{x}$ and $\mathbf{p}_{\boldsymbol{\lambda}}$ are orthogonal, as shown in Figure A-1, we obtain an expression for the reflection angle θ

$$|\tan(\theta)| = \frac{|\mathbf{p}_{\boldsymbol{\lambda}}|}{|\mathbf{p}\boldsymbol{x}|} = \frac{|\mathbf{k}_{\boldsymbol{\lambda}}|}{|\mathbf{k}\boldsymbol{x}|} \tag{A-13}$$

$$= \frac{\sqrt{k_{\lambda_x}^2 + k_{\lambda_y}^2 + k_{\lambda_z}^2}}{\sqrt{k_x^2 + k_y^2 + k_z^2}}\,. \tag{A-14}$$

We can define the azimuthal angle as the angle between any vector that rotates along with the reflection plane and an arbitrary direction. The vector $\mathbf{p}\boldsymbol{x} \times \mathbf{p}_{\boldsymbol{\lambda}}$ is contained in the reflecting plane and rotates 360° with the reflection plane. Let $\mathbf{v}$ be an arbitrary direction, then the azimuthal angle between $\mathbf{p}\boldsymbol{x} \times \mathbf{p}_{\boldsymbol{\lambda}}$ and $\mathbf{v}$ is given by

$$\cos\phi = \frac{(\mathbf{v}) \cdot (\mathbf{p}\boldsymbol{x} \times \mathbf{p}_{\boldsymbol{\lambda}})}{|\mathbf{v}||\mathbf{p}\boldsymbol{x} \times \mathbf{p}_{\boldsymbol{\lambda}}|}\,. \tag{A-15}$$

Here, we choose to define the x-axis (inline) direction as the azimuthal reference direction $\mathbf{v} = (1, 0, 0)$, and the azimuthal angle as the angle between the line of intersection line between the reflection plane and the horizontal x-y plane and the x-axis. One advantage of this choice of reference is that it allows one to study local media property variations in relation to the same direction. One disadvantage of this choice is that this definition breakes down for vertical reflectors because the intersection between all possible reflection planes, at a fixed image point location, and the horizontal plane all have the same direction.

Let vector $\mathbf{d}$ be the cross-product if the vectors $\mathbf{p}_{\boldsymbol{\lambda}}$ and $\mathbf{p}\boldsymbol{x}$,

$$\mathbf{d} = \mathbf{p}_{\boldsymbol{\lambda}} \times \mathbf{p}\boldsymbol{x} \tag{A-16}$$

$$= (p_{\lambda_y} p_z - p_{\lambda_z} p_y, p_{\lambda_z} p_x - p_{\lambda_x} p_z, p_{\lambda_x} p_y y - p_{\lambda_y} p_x)\,. \tag{A-17}$$

As indicated earlier, $\mathbf{d}$ is orthogonal to the reflection plane and it is contained in the reflecting plane. As the reflection plane rotates, the vector $\mathbf{d}$ also rotates, so we can associate the orientation of $\mathbf{d}$ with the orientation of the reflection plane. Let $\mathbf{d}_h = (d_x, d_y, 0)$ be the horizontal projection of $\mathbf{d}$ in the x-y

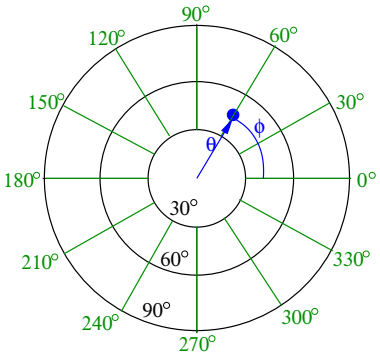

Figure 9. Polar representation of reflection energy function of reflection and azimuthal angle: The azimuthal angle ϕ is zero at the positive horizontal direction and increases in the counter-clockwise direction. The distance from the center of the circles to the event represents the angle θ, which has a minimum value of zero for events appearing in the center of the Figure, and a maximum value of 90 for events located on the outer circle. The filled dot represents a reflection event where $\theta = 45^\circ$ and $\phi = 60^\circ$.

plane. We define the azimuthal angle ϕ as the angle between $\mathbf{d}$ and the inline direction, so

$$\cos\phi = \frac{k_{\lambda_y}k_z - k_{\lambda_z}k_y}{\sqrt{(k_{\lambda_y}k_z - k_{\lambda_z}k_y)^2 + (k_{\lambda_z}k_x - k_{\lambda_x}k_z)^2}} \,. \tag{A-18}$$

Since $\mathbf{k_\lambda}$ and $\mathbf{k_x}$ are orthogonal to each other

$$\mathbf{k_\lambda} \cdot \mathbf{k_x} = k_{\lambda_x}k_x + k_{\lambda_y}k_y + k_{\lambda_z}k_z = 0 \,, \tag{A-19}$$

and

$$k_{\lambda_z} = \frac{-k_{\lambda_x}k_x - k_{\lambda_y}k_y}{k_z} \,. \tag{A-20}$$

Thus, we can eliminate k_{λ_z} from equations A-14 and A-18 and rewrite these equations as

$$\tan\theta = \frac{\sqrt{(k_{\lambda_x}^2 + k_{\lambda_y}^2)k_z^2 + (-k_xk_{\lambda_x} - k_yk_{\lambda_y})^2}}{\sqrt{k_z^2(k_x^2 + k_y^2 + k_z^2)}} \,, \tag{A-21}$$

and

$$\cos\phi = \frac{k_z^2k_{\lambda_y} + k_xk_yk_{\lambda_x} + k_y^2k_{\lambda_y}}{\sqrt{(k_z^2k_{\lambda_y} + k_xk_yk_{\lambda_x} + k_y^2k_{\lambda_y})^2 + (-k_x^2k_{\lambda_x} - k_yk_xk_{\lambda_y} - k_{\lambda_x}k_z^2)^2}} \,. \tag{A-22}$$

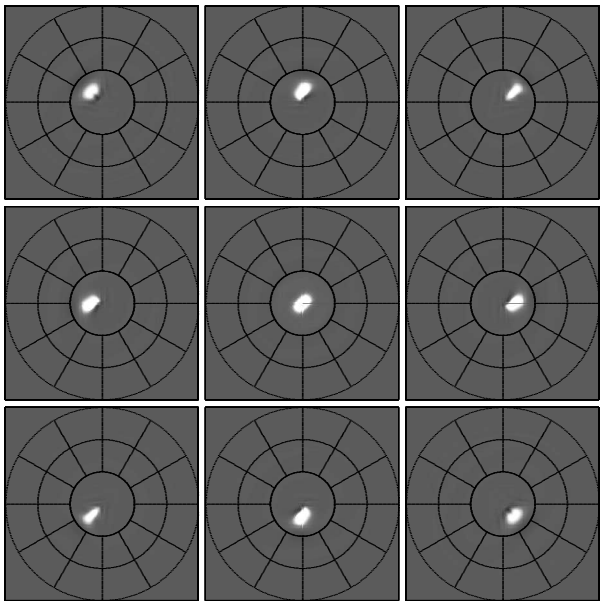

Figure 10. angle-domain common-image gathers: each individual plot is the angle gather (CIG) obtained from the lag gathers in Figure 8. The gathers are displayed in a polar plot format. Refer to Figure 9 for a polar plot interpretation.

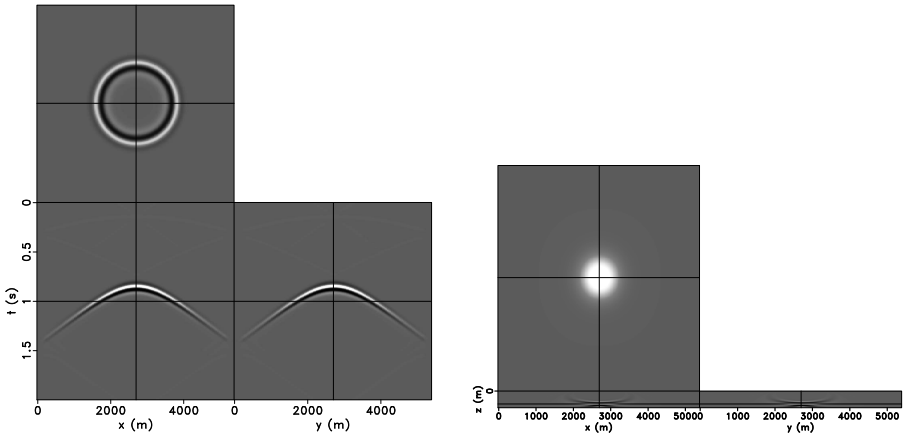

(a) (b)

Figure 11. Data for the one shot located at center of x-axis (a), and image of horizontal reflector located at $z_r = 700$ m (b).

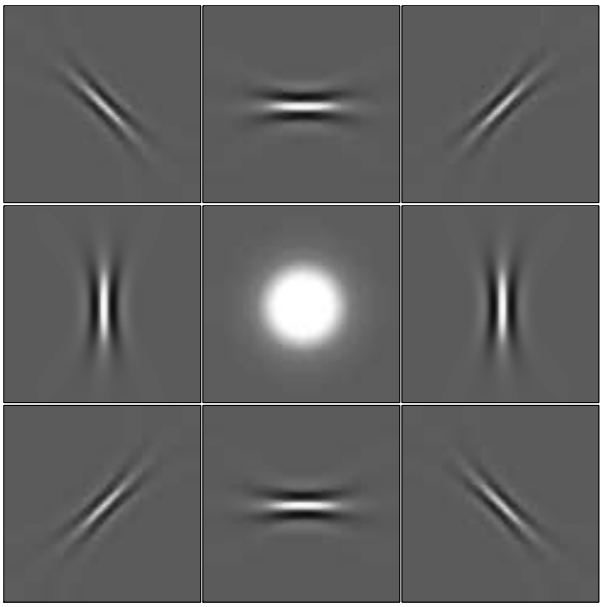

Figure 12. Space-lag domain common-image gathers: each individual plot is a lag gather for a different horizontal location over the reflector. In each Figure, the horizontal axis is λ_x and the vertical is λ_y. The gather in the center has the same horizontal location as the source. The gathers around the central one are located 300 m away from it in one or both horizontal directions.

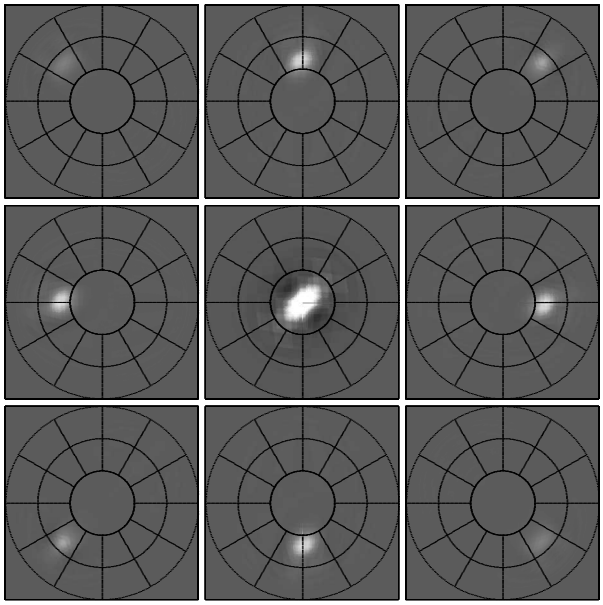

Figure 13. angle-domain common-image gathers: each individual plot is the angle gather (CIG) obtained from the lag gathers in Figure 12. The gathers are displayed in a polar plot format.

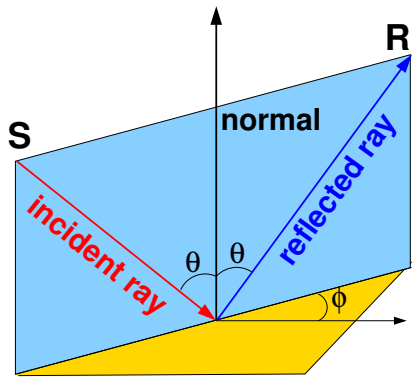

Figure A-1. Geometrical relations between ray parameter vectors.